Semiclassical dynamics of a disordered two-dimensional Hubbard model with long-range interactions

Adam S. Sajna^{1,2} and Anatoli Polkovnikov¹

¹Department of Physics, Boston University, 590 Commonwealth Avenue, Boston, Massachusetts 02215, USA
²Faculty of Physics, Adam Mickiewicz University, Uniwersytetu Poznańskiego 2, 61-614 Poznań, Poland



(Received 20 February 2020; revised 17 August 2020; accepted 19 August 2020; published 28 September 2020)

Quench dynamics in a two-dimensional system of interacting fermions is analyzed within the semiclassical truncated Wigner approximation (TWA). The models with short-range and long-range interactions are considered. We show that in the latter case, the TWA is very accurate, becoming asymptotically exact in the infinite-range limit, provided that the semiclassical Hamiltonian is correctly identified. Within the TWA, different dynamical timescales of charges and spins can be clearly distinguished. Interestingly, for a weak and moderate disorder strength, we observe subdiffusive behavior of charges, while spins exhibit diffusive dynamics. At strong disorder, the quantum Fisher information shows logarithmic growth in time with a slower increase for charges than for spins. It is shown that in contrast to the short-range model, strong inhomogeneities such as domain walls in the initial state can significantly slow down thermalization dynamics, especially at weak disorder. This behavior can put additional challenges in designing cold-atom experimental protocols aimed to analyze possible many-body localization in such systems. While within this approach we cannot make any definite statements about the existence of a many-body localized phase, we see a very fast crossover as a function of disorder strength from rapidly thermalizing to a slow glassylike regime both for the short-range and long-range models.

DOI: 10.1103/PhysRevA.102.033338

I. INTRODUCTION

Understanding the dynamics of isolated interacting disordered many-body systems has recently became a forefront of both theoretical and experimental research [1–15]. Such systems have been explored both with respect to possible applications to quantum information [12,13] and as generic models of possible ergodicity breaking in interacting systems [14,16]. It is well known that a competition of interaction and disorder leads to a peculiar dynamical behavior of the entanglement entropy and information propagation [3,11,12,17– 20]. In particular, this dynamical behavior can be highly sensitive to the interaction range [21–25]. Disordered systems with long-range interaction have already been realized in experiments with trapped ions [3,5]. There also exist solid-state disordered materials with long-range Coulomb interactions [26]. Electrons in such materials are strongly localized and charge carries cannot screen long-range interactions, making their long-range nature play a very important role. Coulomb interactions also remain unscreened in two-dimensional materials such as suspended graphene [27]. There is thus a very clear need for the development of efficient theoretical methods which could simulate such systems in any dimension.

Conceptually, the interplay of disorder and interactions can be understood within the framework of the Hubbard model [28]. Originally introduced as a toy model to understand interacting systems, it has been experimentally realized in different spatial dimensions. In particular, a realization of a disordered or quasiperiodic Hubbard model in one and two spatial dimensions has been reported in Refs. [1,4,8,9,15]. In several recent works, it has been argued that two-component fermions might not have the many-body localized phase in one spatial dimension due to the coexistence of spin and charge excitations [29–36]. In particular, charge and spin degrees of freedom can exhibit different localization properties and affect long-time dynamics [37,38].

In this paper, we systematically analyze quantum dynamics in an interacting fermionic Hubbard model with long-range interactions using the fermionic version of the truncated Wigner approximation (fTWA) [39,40]. We focus on twodimensional (2D) systems, but also mention some results in the one-dimensional (1D) case, mostly to benchmark the approach against the exact diagonalization. We show that for the accuracy of the method, it is crucial to choose the correct representation of the Weyl symbol of the Hamiltonian and of the observables. In particular, the fermionic number operator $\hat{n}_{\alpha} = \hat{c}_{\alpha}^{\dagger} \hat{c}_{\alpha}$, where α is some index labeling of the corresponding single-particle state, always satisfies the identity $\hat{n}_{\alpha}^2 = \hat{n}_{\alpha}$. At the same time, the Weyl symbols of \hat{n}_{α} and \hat{n}_{α}^2 are different. Thus there is an ambiguity in defining the phasespace representation of the corresponding operators. Within the exact analysis of the dynamics, this ambiguity is irrelevant, but within the semiclassical TWA approximation it plays a significant role. In this paper, we remove the ambiguity by choosing the representation of the Hamiltonian, which leads to asymptotically exact fTWA dynamics when the range of interactions becomes infinite. It is shown that the choice of this particular representation also leads to a dramatic improvement in the accuracy of fTWA over a more naive representation if interactions decay as a power law. We note that such an

ambiguity might exist for other setups, e.g., spin-1/2 systems, where the spin operators satisfy similar identities: $\hat{s}_{x,y,z}^2 = \hat{I}/4$. Our work suggests that in those situations, choosing the right representation of the Hamiltonian can significantly improve the accuracy of TWA.

Using this improved representation, fTWA was applied to analyze the charge and spin dynamics in the long-range interacting systems. In particular, we study transport and timedependent correlation functions and the role of disorder and interactions. It is found that within fTWA it is possible to clearly distinguish different dynamical timescales in the transport of charge and spin degrees of freedom. For weak and moderate disorder strength, the charges exhibit subdiffusive dynamics, while the spin dynamics remains nearly diffusive. This separation of timescales is related to the fact that both spin components are subject to the same disorder potential. For strong disorder, both charge and spin are nearly localized, undergoing very slow glassy dynamics. In this regime, the quantum Fisher information (QFI) is shown to be a good indicator of the timescales associated with spin and charge sectors. Such QFI has been recently measured in a quantum simulator of a one-dimensional disordered spin system with long-range interactions [3]. We observed a logarithmic growth of QFI for both degrees of freedom. However, the growth rate for charges is slower than for spins, which is consistent with a stronger tendency of localization of the charge degrees of freedom. This difference disappears in the noninteracting limit, in which the system exhibits the Anderson localization reflected in a rapid saturation of QFI [20,24]. Moreover, in contrast to the Hubbard model with short-range interactions, strong inhomogeneities in the initial state like that used in the short-range systems (Ref. [2]) is found to significantly slow down the dynamics, even at weak disorder. Thus, in the long-range systems, extra care should be taken to choose the right initial state needed to check the possible existence of many-body localization.

Most of the numerical studies are performed for 2D square lattices, which are intractable by exact methods. While we cannot definitely address all questions, in particular whether the system can be in a localized state beyond some disorder threshold, we can extract many quantitative and qualitative features of the dynamics in such systems, showing the power of the fTWA approach to study cold-atom systems and possibly even real materials.

The rest of the paper is organized as follows. In Sec. II, the semiclassical fTWA method and, in particular, its implementation in the Hubbard model are discussed. In Secs. III and IV, we analyze charge and spin transport in the presence of quenched disorder. In Sec. V, the impact of different initial conditions on transport and thermalization timescales is revealed. In the last section, we summarize our results. Additional technical details of the fTWA method are discussed in the Appendices.

II. fTWA IMPLEMENTATION OF THE HUBBARD MODEL

Semiclassical representation of fermionic dynamics within the fTWA in terms of phase-space stringlike variables was recently exploited in Refs. [39,40]. These string variables can be introduced through Weyl symbols of the following bilinear operators:

$$\hat{\hat{E}}^{\alpha}_{\beta} = \frac{1}{2} (\hat{c}^{\dagger}_{\alpha} \hat{c}_{\beta} - \hat{c}_{\beta} \hat{c}^{\dagger}_{\alpha}), \ \hat{E}_{\alpha\beta} = \hat{c}_{\alpha} \hat{c}_{\beta}, \ \hat{E}^{\alpha\beta} = \hat{c}^{\dagger}_{\alpha} \hat{c}^{\dagger}_{\beta} = -\hat{E}^{\dagger}_{\alpha\beta},$$

$$\tag{1}$$

where $\hat{c}_{\alpha}^{\dagger}$ and \hat{c}_{α} , $\alpha = \{i, \sigma\}$ are the fermionic creation and annihilation operators, where i is the site position and σ is the spin index. These bilinear operators generate the SO(2N) group and their corresponding Weyl symbols are $\rho_{\alpha\beta} = (\hat{E}_{\beta}^{\alpha})_{W}$, $\tau_{\alpha\beta} = (\hat{E}_{\alpha\beta})_{W}$, $-\tau_{\alpha\beta}^{*} = (\hat{E}^{\alpha\beta})_{W}$, which satisfy canonical Poisson bracket relations with the structure constants of this SO(2N) group [39]. In addition, the subset of number-conserving operators \hat{E}_{β}^{α} serve as generators of the U(N) subgroup of SO(2N). Using phase-space representation of the operators and the Hamiltonian in terms of $\rho_{\alpha\beta}$ and $\tau_{\alpha\beta}$, one can define the dynamics within fTWA, which is a straightforward generalization of the classical dynamics of coupled rigid rotators (see, also, Appendix A).

In Ref. [39], it was shown that phase-space (Weyl) representation of the interaction term in the Hamiltonians can lead to ambiguities. For example, two-particle interactions in the Hubbard model of the type

$$U_{\alpha\beta\gamma\delta}\hat{c}_{\alpha}^{\dagger}\hat{c}_{\beta}^{\dagger}\hat{c}_{\gamma}\hat{c}_{\delta} \tag{2}$$

can be represented either through a product of the operators $\hat{E}^{\alpha}_{\delta}$ and \hat{E}^{β}_{γ} (permutation of indexes α, β or γ, δ leads to an equivalent representation [39]) or, alternatively, through a product of operators $\hat{E}^{\alpha\beta}$ and $\hat{E}_{\gamma\delta}$. In the first representation, the Weyl symbol of the Hamiltonian is represented entirely through ρ variables, while in the second representation, the Hamiltonian is generally expressed through both ρ and τ variables. These two different representations are not equivalent and while in some situations the first ρ representation gives an accurate description of the dynamics within the fTWA, in other situations, such as for the Sachdev-Ye-Kitaev (SYK) model, the second ρ , τ representation leads to an accurate (and even asymptotically exact) fTWA description [39,40]. In a way, a choice of representation in fTWA is similar to the choice of a particular decoupling in mean-field approximations. Here we show that even if we focus on the first ρ representation, there are still some ambiguities in rewriting the interaction term. We use this ambiguity to our advantage, significantly improving the accuracy of simulations of the semiclassical many-body dynamics in systems with longrange interactions.

This new ambiguity comes from noticing that the quantum operators $\hat{n}_{i\sigma}$ and $\hat{n}_{i\sigma}^2$, where $\hat{n}_{i\sigma} = \hat{c}_{i\sigma}^{\dagger} \hat{c}_{i\sigma}$, are identical. However, the Weyl symbols for these two operators lead to different phase-space representations of the corresponding terms. In particular,

$$\hat{n}_{i\sigma} \to \rho_{i\sigma i\sigma} + 1/2, \quad \hat{n}_{i\sigma}^2 \to (\rho_{i\sigma i\sigma} + 1/2)^2.$$
 (3)

Generally, within the semiclassical dynamics, there is no conservation law of the single cite occupation number $\rho_{i\sigma i\sigma}$ because this conservation law does not originate from the corresponding Lie algebra, but rather from its particular (fundamental) representation. A simple way to see this inequivalence is to observe that if the Hamiltonian contains the corresponding $\hat{n}_{i\sigma}$ term, then the second representation leads to nonlinear equations of motion within the fTWA, while the first representation keeps equations linear. In the following,

we explain that this ambiguity can be resolved by requiring that the fTWA becomes exact in the limit of infinite-range interactions. It is found that the corresponding representation also significantly improves the accuracy of the fTWA for algebraically decaying long-range interactions.

In this work, we focus on the Hubbard Hamiltonian with long-range interactions,

$$\hat{H}_{I} = -J \sum_{\langle ij \rangle \sigma} (\hat{c}_{i\sigma}^{\dagger} \hat{c}_{j\sigma} + \text{H.c.}) + \sum_{i\sigma} \Delta_{i} \hat{n}_{i\sigma} + \sum_{ij} U_{ij} \hat{n}_{i\uparrow} \hat{n}_{j\downarrow} + \sum_{i < i\sigma} V_{ij\sigma} \hat{n}_{i\sigma} \hat{n}_{j\sigma},$$
(4)

where J is the spin-independent hopping amplitude between neighboring sites, Δ_i is the on-site disorder potential with the strength uniformly distributed in the range $\Delta_i \in [-\Delta, \Delta]$, and U_{ij} ($V_{ij\sigma}$) is the density-density interaction coupling between different (identical) spin components. We assume that these interparticle interactions are translationally invariant and depend only on the distance between the particles: $U_{ij} = U(|\mathbf{r}_i - \mathbf{r}_j|)$ and $V_{ij\sigma} = V_{\sigma}(|\mathbf{r}_i - \mathbf{r}_j|)$ (\mathbf{r}_i is a real-space vector corresponding to the location of the site i). Open boundary conditions are used.

While identical fermions cannot interact on the same site due to the Pauli principle, we can formally add this selfinteraction without affecting the dynamics by considering a different Hamiltonian instead,

$$\hat{H}_{II} = -J \sum_{\langle ij \rangle \sigma} (\hat{c}_{i\sigma}^{\dagger} \hat{c}_{j\sigma} + \text{H.c.}) + \sum_{i\sigma} \Delta_{i} \hat{n}_{i\sigma}$$

$$+ \sum_{ij} U_{ij} \hat{n}_{i\uparrow} \hat{n}_{j\downarrow} + \frac{1}{2} \sum_{ij,\sigma} V_{ij\sigma} \hat{n}_{i\sigma} \hat{n}_{j\sigma}$$

$$= \hat{H}_{I} + \underbrace{\frac{1}{2} \sum_{\sigma} V_{0\sigma} \sum_{i} \hat{n}_{i\sigma}^{2}}_{\frac{1}{2} V_{0\uparrow} \hat{N}_{\uparrow} + \frac{1}{2} V_{0\downarrow} \hat{N}_{\downarrow}}$$
(5)

where $V_{0\sigma} \equiv V_{\sigma}(|\mathbf{r}_i - \mathbf{r}_i| = 0)$. The difference between the two Hamiltonians is proportional to terms with a conserved number of fermions in each spin degree of freedom,

$$\hat{H}_{II} - \hat{H}_{I} = \frac{1}{2} V_{0\uparrow} \hat{N}_{\uparrow} + \frac{1}{2} V_{0\downarrow} \hat{N}_{\downarrow}, \quad \hat{N}_{\sigma} = \sum_{i} \hat{n}_{i\sigma}, \quad (6)$$

which commutes \hat{H}_I and, hence, both Hamiltonians lead to identical quantum dynamics. However, these two Hamiltonians lead to different semiclassical approximations. In the next section (Sec. III), we show that fTWA based on \hat{H}_{II} leads to much more accurate predictions. Intuitively, this improvement follows from considering infinite-range interactions where U_{ij} , $V_{ij\sigma}$ are independent of $\mathbf{r}_i - \mathbf{r}_j$. In this case, it is easy to check (see Appendix B for details) that the interaction term commutes with the rest of the Hamiltonian and drops out from the equations of motion. However, within the fTWA, the interaction term in this limit only drops if we use the Weyl representation of \hat{H}_{II} , but not \hat{H}_I . We checked that for the systems with short-range interactions, both Weyl representations lead to similar results.

In the rest of the paper, we focus on the situation $U_{ij} = V_{ij\sigma}$ corresponding to an additional SU(2) spin symmetry [41,42].

We also consider long-range power-law interactions such that

$$U_{ij} = V_{ij\sigma} = \frac{U}{|\mathbf{r}_i - \mathbf{r}_j|^{\alpha}}, \quad i \neq j, \tag{7}$$

and, for on-site interactions, $U_{ii} = V_{ii\sigma} = U$ is taken. As we already pointed out in the infinite-range case $\alpha = 0$, the dynamics of the system becomes effectively noninteracting, i.e., equivalent to U = 0, because in this case the interaction term simply reduces to the square of the total number of fermions with factor U.

III. BENCHMARKING ACCURACY OF THE FTWA IN ONE DIMENSION

Before proceeding with analyzing dynamics in twodimensional systems, we will check the accuracy of fTWA and the differences between the two semiclassical representations of the quantum Hamiltonian in smaller one-dimensional systems. In particular, we will analyze the quench dynamics in the half-filled one-dimensional lattice of eight sites with open boundary conditions. Such a system is amenable to exact-diagonalization methods and hence can be used to test the semiclassical method. Following recent cold-atom experiments [1,2,4,8], we will study the dynamics of the spin and charge imbalance after quenching from a charge or spin density wave state. This imbalance serves as a good indicator of ergodicity in the system. At strong disorder, where the imbalance does not decay in time due to localization, a more sensitive probe distinguishing the dynamics of interacting and noninteracting systems is the quantum Fisher information (QFI), which was recently measured for long-range interacting ions in the presence of disorder [3]. Like entanglement, the OFI can distinguish between a noninteracting Anderson localization mechanism [43] and possible many-body localization (MBL) [18,44,45]. The details of implementation of the fTWA method are described in Appendices A and B.

To study the dynamics of charge and spin degrees of freedom, we prepare the system in a charge density wave (CDW) and spin density wave (SDW), respectively. For the charge dynamics, we consider a pure initial state,

$$|\Psi_{\text{init}}^{C}\rangle = |0, \uparrow\downarrow, 0, \uparrow\downarrow, \dots\rangle,$$
 (8)

and for spin dynamics, we start from a different initial state,

$$|\Psi_{\text{init}}^{S}\rangle = |\downarrow, \uparrow, \downarrow, \uparrow, \dots\rangle.$$
 (9)

As observables, we choose the charge $[z_C(t)]$ and the spin $[z_S(t)]$ imbalances normalized to the total number of fermions N, which we define as

$$z_C(t) = \frac{1}{N} \langle \hat{Z}_C(t) \rangle = \frac{1}{N} \sum_i (-1)^i \langle \Psi_{\text{init}}^C | \hat{n}_i(t) | \Psi_{\text{init}}^C \rangle$$
 (10)

and

$$z_{S}(t) = \frac{1}{N} \langle \hat{Z}_{S}(t) \rangle = \frac{1}{N} \sum_{i} (-1)^{i} \langle \Psi_{\text{init}}^{S} | \hat{m}_{i}(t) | \Psi_{\text{init}}^{S} \rangle, \quad (11)$$

where $\hat{n}_i = \hat{n}_{i\uparrow} + \hat{n}_{i\downarrow}$ and $\hat{m}_i = \hat{n}_{i\uparrow} - \hat{n}_{i\downarrow}$ are the on-site charge density and the on-site spin polarization, respectively. In a two-dimensional square lattice, analyzed in Sec. IV, we replace $(-1)^i$ with $(-1)^{i_x}$, where i_x and i_y are the integer site indexes along the x and y directions.

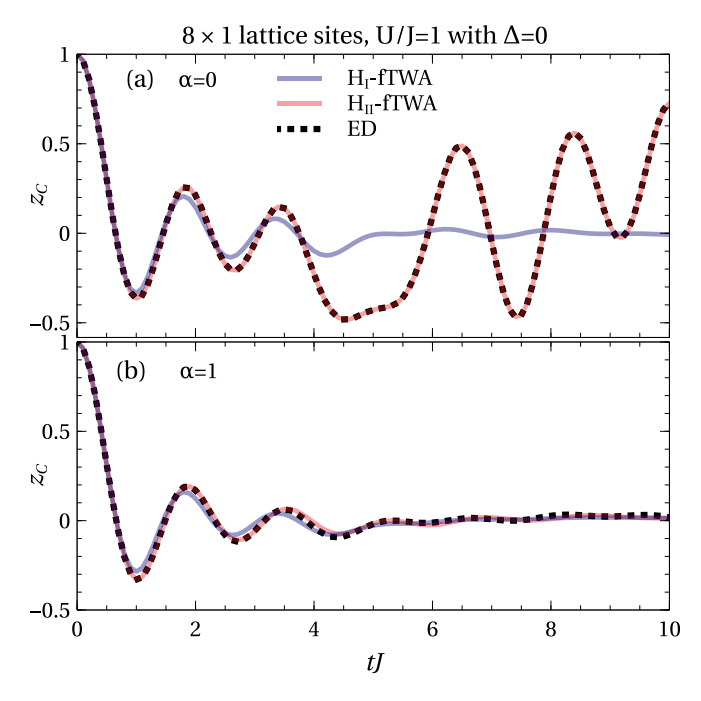


FIG. 1. Time dependence of the charge imbalance z_C [cf. Eq. (10)] for the initial CDW state. The black dashed line represents the exact-diagonalization (ED) results, while the solid blue (dark gray) and the solid red (light gray) lines represent the results of the fTWA method based on the Hamiltonians \hat{H}_I and \hat{H}_{II} , respectively. (a) The infinite-range interactions ($\alpha=0$); (b) the interactions decaying with the power $\alpha=1$. All simulations are obtained on a system consisting of 8-lattice sites at half filling with U/J=1 in the absence of disorder ($\Delta=0$).

For a pure initial state, we will also study the normalized QFI corresponding to the charge and spin imbalance operators \hat{Z}_C and \hat{Z}_S [3,20,24,46–49]:

$$f_{Q,C/S}(t) = \frac{4}{N} \left[\left\langle \hat{Z}_{C/S}^2(t) \right\rangle - \left\langle \hat{Z}_{C/S}(t) \right\rangle^2 \right]. \tag{12}$$

We stress that it is the presence of quantum noise that is essential to get the nontrivial QFI in the fTWA method. In the mean-field approximation, which is equivalent to the fTWA if we suppress all the noise to zero, $f_{Q,C/S}(t) \equiv 0$ because there are no fluctuations and, hence, $\langle \hat{Z}_{C/S}^2(t) \rangle = \langle \hat{Z}_{C/S}(t) \rangle^2$. On top of quantum averaging, we will also perform averaging of the observables over different disorder realizations, which we denote by an overline and show numerical results for $\bar{z}_{C/S}$, $\bar{f}_{Q,C/S}$.

First let us analyze the charge imbalance $z_C(t)$ starting from the initial CDW state. In Fig. 1, we show a comparison of the ED and fTWA dynamics for a nondisordered lattice $(\Delta = 0)$. Figures 1(a) and 1(b) correspond to the infinite interaction range $(\alpha = 0)$ and the interactions proportional to the inverse distance $(\alpha = 1)$. As we discussed in Sec. II, fTWA based on \hat{H}_{II} (H_{II} -fTWA) is exact for $\alpha = 0$ for any system size. In comparison, the fTWA based on \hat{H}_{I} (H_{I} -fTWA) is only accurate for relatively short times. In the case of power-law interactions, the system is nonintegrable and generally exhibits thermalization [Fig. 1(b)]. In this case, both representations of the fTWA give similar accurate predictions of the charge

imbalance decay with H_{II} -fTWA still overperforming the H_{I} -fTWA. We checked that the situation is similar for the spin imbalance $z_S(t)$.

As we increase the disorder strength, the improvement of the H_{II} -fTWA over the H_{I} -fTWA becomes even more significant, especially at longer times. This is illustrated in Fig. 2, where we plot $z_{C/S}$ and $f_{Q,C/S}$ for a fixed power $\alpha=1$. Here the upper panels represent the results for the charges and the lower panels correspond to spins. Figures 2(c) and 2(f) show the mean-square error (MSE) of the fTWA simulations as a function of the disorder strengths. The MSE is defined as

$$\frac{1}{M} \sum_{i=1}^{M} \left[\bar{z}_{C/S}^{\text{ED}}(t_i) - \bar{z}_{C/S}^{fTWA}(t_i) \right]^2$$
 (13)

for the charge or spin imbalance, and

$$\frac{1}{M} \sum_{i=1}^{M} \left[\bar{f}_{Q,C/S}^{\text{ED}}(t_i) - \bar{f}_{Q,C/S}^{fTWA}(t_i) \right]^2 \tag{14}$$

for the QFI. Here, M is the total number of time simulation steps within the time interval $t_i J \in [0, 200]$. From Figs. 2(c) and 2(f), we see that the fTWA gives satisfactory predictions both for short- and long-time dynamics in the limits of weak $(\Delta/J \approx 1)$ and strong $(\Delta/J \gg 1)$ disorder potentials. In the intermediate disorder regime, the fTWA introduces a significant error. This situation is qualitatively similar to the one for spin systems [50,51]. At these intermediate disorder strengths, the semiclassical dynamics clearly leads to faster thermalization than exact quantum dynamics. A possible explanation for why classical systems thermalize faster was given in Ref. [52]. There the authors argued that it is discreteness of quantum levels, which further suppresses slow classical transport through chaotic resonances. While it is unclear how these considerations extend to fTWA, which deals with nonlocal bilinears, qualitatively the situation is very similar. We point out that fTWA shows a stronger tendency to localization than, e.g., the cluster TWA. It is possible that the accuracy of fTWA can be further improved by choosing a more efficient operator basis, e.g., the basis of l-bits [53], which is obtained by a local unitary transformation of the local fermion basis. Unitary transformations do not change the commutation relations of the basis operators and, hence, the dressed operators still form a closed algebra and can be used to construct dressed versions of fTWA. This possibility needs further investigation, which is beyond the scope of the current manuscript.

It is also interesting to point out that both the ED and the fTWA (cf. Fig. 2) show that spin degrees of freedom tend to thermalize faster than charges. A similar tendency was also observed in several recent papers [29–33,35–38]. The reason behind the asymmetry between spin and charge degrees of freedom is that the Hamiltonian (5) introduces only disorder in the charge sector, allowing spins to delocalize much faster. In order to localize spins, one can introduce additional disorder in the spin channel [29,35]. We checked that this is indeed correct in Sec. IV, where charge and spin dynamics in the two-dimensional setup are discussed.

From the MSE, it is also seen that the H_{II} -fTWA is generally more accurate in predicting both the imbalance and the QFI, especially in the crossover region [cf. Figs. 2(c)

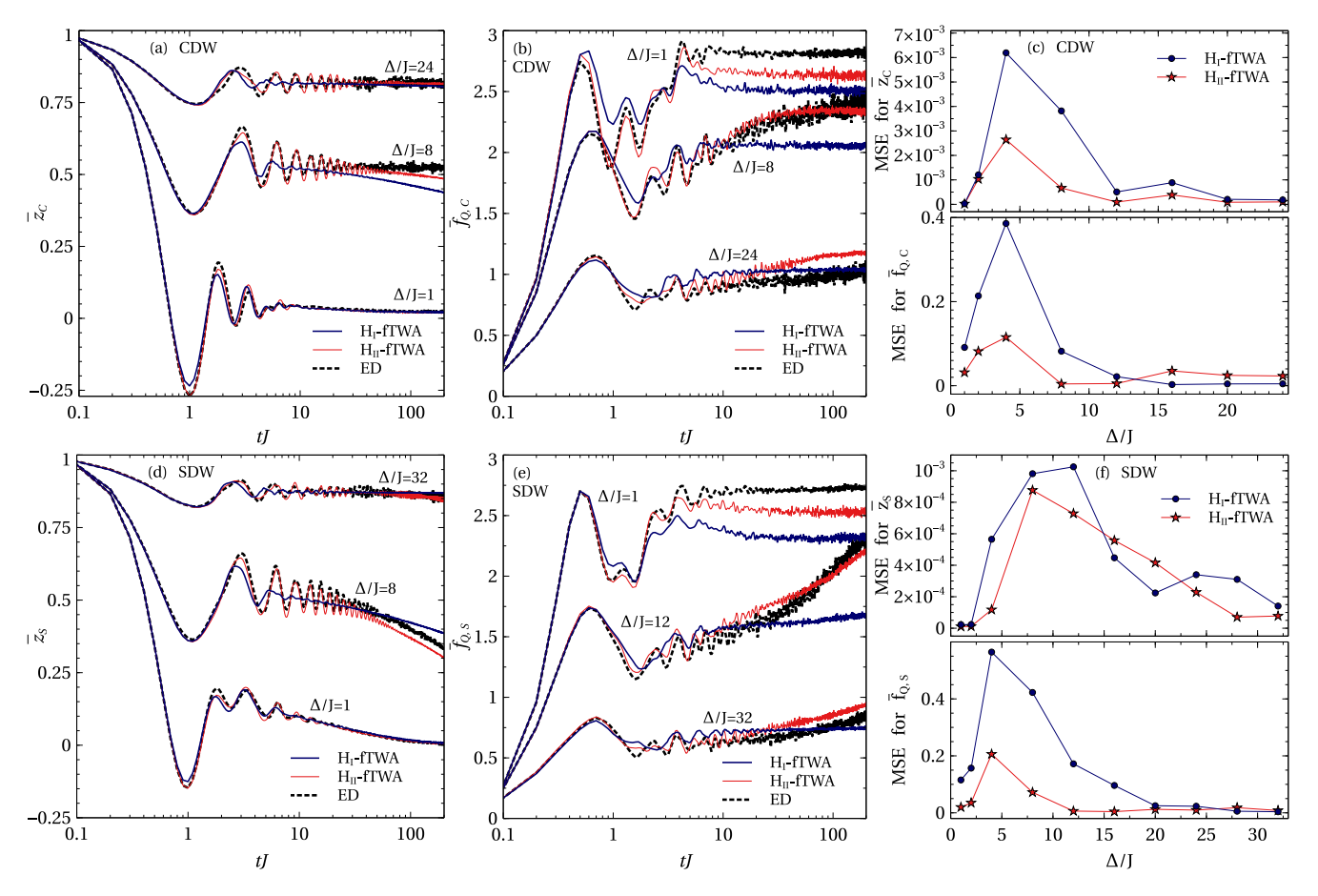


FIG. 2. Time dependence (a),(d) of the imbalance $z_{C/S}$ and (b),(e) of the QFI $f_{C/S}$ for different disorder strengths Δ/J . Simulations are done for a 1D system of size 8 and open boundary conditions. The top and bottom rows correspond, respectively, to the CDW and SDW initial states (see text for details). The solid blue (dark gray) and red (light gray) lines represent simulations done with H_I – fTWA and H_{II} – fTWA, respectively; the black dashed line shows ED simulations. (c),(f) The mean-square error (MSE) of the two fTWA approximations. All the results were averaged over 100 different disorder realizations. The remaining parameters of the Hamiltonian are U/J = 1, $\alpha = 1$.

and 2(f)]. Also, the H_{II} -fTWA is able to capture the initial transient imbalance oscillations up to longer times ($tJ \approx 10$) as compared to the H_I -fTWA, which agrees with the ED only up to $tJ \approx 3$.

Next, we analyze the accuracy of the fTWA as we vary the exponent α . As we mentioned in Sec. II, H_{II} -fTWA should approach the exact results for $\alpha \to 0$. We only consider the behavior of the charge imbalance $z_C(t)$ and $f_C(t)$ (the behavior of the spin imbalance is qualitatively similar), which is shown in Fig. 3 for a fixed quenched disorder with the strength $\Delta/J = 8$. At this strong disorder, the charge transport is suppressed, and yet the imbalance changes significantly compared to its initial value. Within the ED, the charge imbalance $z_C(t)$ is nearly identical for all three considered values of $\alpha = 0, 0.25, 1$, while the QFI information clearly distinguishes the infinite-range $\alpha = 0$ regime from the other two. In all three cases, the H_{II} -fTWA gives more accurate results than the H_I -fTWA. As expected, the H_{II} -fTWA becomes asymptotically exact as the exponent α approaches zero; in particular, for $\alpha = 0.25$, the charge imbalance $z_C(t)$ is nearly exactly reproduced by the H_{II} -fTWA. These observations are also consistent with the analytical considerations presented in Appendix B. Differences between the two fTWA simulations and the ED are even more pronounced for the QFI [Figs. 3(d)–3(f)]. In particular, the H_I -fTWA is not able to predict the long-time behavior of the QFI for all values of α , while the H_{II} -fTWA yields significantly more accurate results.

It is worthwhile to add that the H_{II} -fTWA also slightly improves predictions for the long-time dynamics of the imbalance in the Hubbard model with short-range (on-site) interactions (i.e., $U_{ij} = V_{ij\sigma} = 0$ for $i \neq j$ and $U_{ii} = V_{ii\sigma} = U_0 \neq 0$). We checked this for the charge imbalance function; see Fig. 4. The improvement is observed for the higher disorder strengths, but it is not so pronounced as in the long-range case. Perhaps the lack of significant improvement of fTWA in the short-range model is expected as both fTWA representations become exact in the noninteracting limit $U_0 = 0$ and none of them is favored over the other when interactions become large. On the contrary, for the long-range model, H_{II} -fTWA is significantly favored over H_I -fTWA by the proximity to the infinite-range model ($\alpha = 0$), where H_{II} -fTWA is exact, while H_I -fTWA is not (see Appendix B for details).

IV. CHARGE AND SPIN DYNAMICS IN TWO DIMENSIONS

We now proceed to analyze the two-dimensional Hubbard Hamiltonian, where the ED is limited to very small system sizes such that any extrapolation to the thermodynamic limit

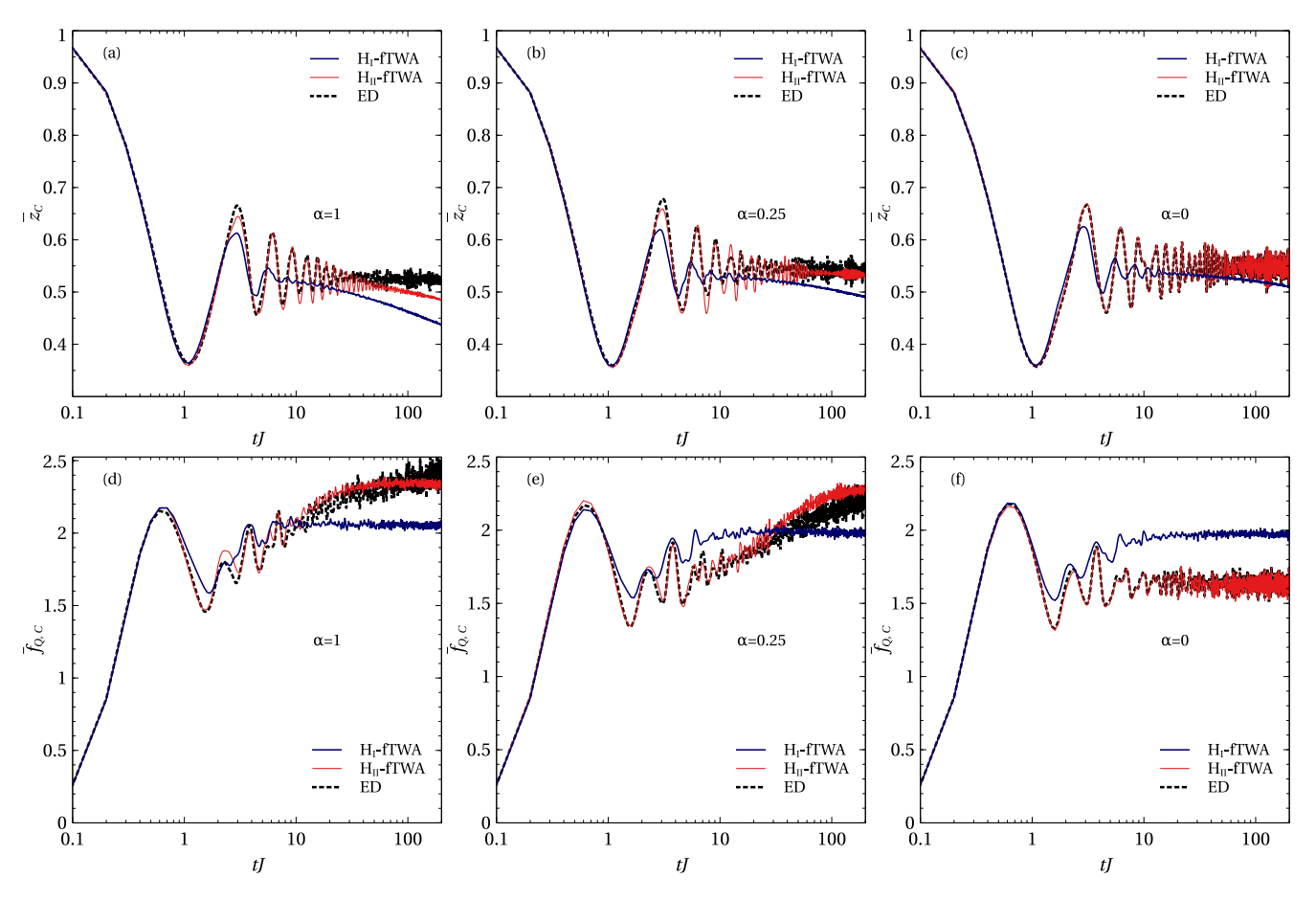


FIG. 3. Time dependence of the (a)–(c) charge imbalance function $z_C(t)$ and the (d)–(f) QFI density $f_{Q,C}$. Simulations are done for a 1D system with eight sites and open boundary conditions. The system is initially prepared in a CDW state (every even side is doubly occupied). The interaction strength is U/J=1 with (a),(d) $\alpha=1$, (b),(e) $\alpha=0.25$, and (c),(f) $\alpha=0$. Moreover, the H_I – fTWA data are represented by the blue (dark gray) line, H_{II} – fTWA by the red solid (light gray) line, and ED by the black dashed line. All the results were averaged over at least 100 disorder potentials with the strength $\Delta/J=8$.

is nearly impossible. In what follows, we present the results of numerical simulations for a 6×6 square lattice using the H_{II} fTWA. Note that while these system sizes are far beyond reach of the ED, they are still relatively small and computationally demanding even within the fTWA approach. The reason is that the fTWA implementation requires one to solve a system of coupled nonlinear differential equations with the number of degrees of freedom scaling as the square of the number of sites in the system (i.e., with the fourth power of the linear system size). It is highly plausible that one can go to larger system sizes by introducing further approximations into solving these nonlinear equations, such as an effective media approximation beyond a certain distance, but the corresponding analysis lies beyond the scope of our work. As we will see, even for such system sizes, we can effectively suppress finite-size effects and make statements about the thermodynamic limit. We focus on the same observables as in the previous section, namely, on the charge and spin imbalances $z_{C/S}(t)$ and the corresponding QFI $f_{C/S}(t)$.

We consider the initial striped CDW or SDW configurations, where the stripes are oriented along the y axis and have a fixed period two along the x axis [see the insets in Figs. 8(a) and 8(c)]. These initial states are obtained from those used earlier in one-dimensional systems [cf. Eqs. (8) and (9)] by adding more rows of lattice sites. We define the charge and spin imbalance operators as

$$\hat{Z}_C(t) = \sum_{i_x i_y} (-1)^{i_x} \hat{n}_{i_x i_y}$$
 (15)

and

$$\hat{Z}_{S}(t) = \sum_{i,i} (-1)^{i_{x}} \hat{m}_{i_{x}i_{y}}, \tag{16}$$

where i_x , i_y are the x and y coordinates of the lattice site $i = (i_x, i_y)$ and $\hat{n}_i = \hat{n}_{i\uparrow} + \hat{n}_{i\downarrow}$, $\hat{m}_i = \hat{n}_{i\uparrow} - \hat{n}_{i\downarrow}$. As before, we use the notations $\bar{z}_C(t)$ and $\bar{z}_S(t)$ for the disorder-averaged expectation values of these operators normalized by the total number of sites. Similarly, we define the corresponding charge and spin QFI according to Eq. (12). All the expectation values are calculated either with the initial CDW or the initial SDW configurations. At half filling, these configurations correspond to $z_{C/S}(t=0)=1$.

In Fig. 5, we plot the results of simulations of the long-time dynamics of the imbalances and the QFI. These plots correspond to the interaction strength U/J=1 and the exponent $\alpha=1$. Similarly to the 1D results discussed in Sec. III, we observe the decay of charge and spin imbalances for any

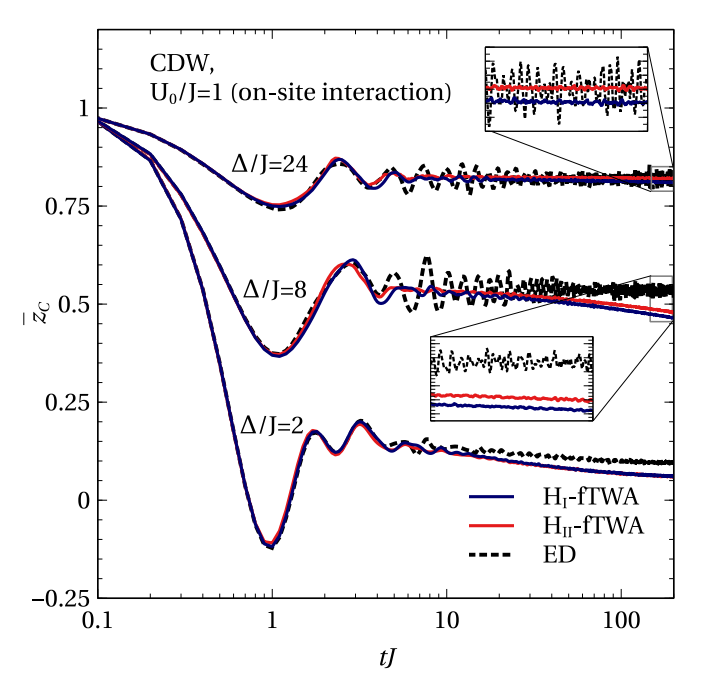


FIG. 4. Time dependence of the charge imbalance function $z_C(t)$. Simulations are done for a 1D system of size 8 with open boundary conditions. The system is initially prepared in the CDW state (every even site is doubly occupied) and the interactions are short range (on-site, i.e., $U_{ij} = V_{ij\sigma} = 0$ for $i \neq j$ and $U_{ii} = V_{ii\sigma} = U_0 \neq 0$). The interaction strength is $U_0/J = 1$. The H_I – fTWA data are represented by the blue (dark gray) lines, the H_{II} – fTWA data by the red (light gray) lines, and the ED data by the black dashed lines. The results were averaged over at least 100 disorder potentials with the strengths $\Delta/J = 24$, 8, 2 (from top to bottom).

disorder strength. As expected at higher disorder, the decay of the charge and spin imbalances is more suppressed. Interestingly, essentially at all values of the disorder potential, charge transport exhibits subdiffusive behavior: $\bar{z}_C \sim t^{-\beta}$, $0 < \beta <$ 1, while the spin dynamics is nearly always diffusive: $\bar{z}_S \approx t^{-1}$ with stronger disorder resulting only in a longer approach to the asymptotic diffusive regime. Thus, our results clearly demonstrate stronger and qualitatively different transport suppression in the charge channel. Qualitatively, the situation is similar to that in one dimension discussed in the previous section (cf. Fig. 2) and in the literature [29–33,35–38], but the difference between the two is more pronounced. Our findings are also consistent with the findings of Ref. [54], where subdiffusive dynamics was observed in a short-range Hubbard model at the infinite-temperature limit using self-consistent perturbation theory.

As in the one-dimensional case, the QFI serves as a good indicator of information spreading due to interactions even when the charge and spin degrees of freedom are nearly localized, clearly distinguishing the interacting system from the Anderson insulator [3,20,24]. In Figs. 5(c) and 5(d), we show the charge and spin QFI density for different disorder strengths Δ/J and for U/J=1, $\alpha=1$. In both the charge and the spin sectors, we observe a very fast (at $tJ\approx 1$) saturation of the QFI at low disorder ($\Delta/J \leq 4$). With increasing disorder, the dynamics of the QFI slows down, approaching the

logarithmic in time growth at strong disorder [see, e.g., the QFI data for $\Delta/J=24$ in Figs. 5(c) and 5(d)]. At the same value of disorder, the spin QFI grows at a faster rate than the charge QFI [cf. black lines in Figs. 5(c) and 5(d)] and reaches the saturation value earlier at $tJ\approx 600$. From these simulations, we can conclude that the information propagation is faster in the spin channel consistent with the faster imbalance decay there.

Next we analyze the QFI propagation through the system, varying the range of interactions. In Fig. 6, we show the corresponding time dependences of the QFI for $\alpha = 0$, 0.25, and 1. Interestingly, even for $\alpha = 0.25$, i.e., for interactions which decay in space very slowly, we still observe very pronounced logarithmic growth of the QFI both for charges and for spins. Interestingly, the anisotropy of the decay times between charge and spin sectors gets larger at smaller values of α . These results suggest that as the interaction range increases, the charge sector is localized especially strongly. We note that the fTWA is expected to be nearly exact for $\alpha = 0.25$ (see Sec. III). As anticipated, after transient behavior, the QFI growth rate for spins and charges decreases with lowering α . This happens because the system is quickly approaching a noninteracting limit ($\alpha = 0$) for which its ability to store new information is lower, i.e., the system becomes less complex. Exactly at $\alpha = 0$, QFI saturates immediately after the transient growth. This dynamics of QFI is aligned with the dynamics of charge and spin imbalances shown in the insets in Fig. 6. For the noninteracting case ($\alpha = 0$), imbalances do not decay because the system is in the regime of Anderson localization. As α increases, the imbalances start to decay because of the additional charge and spin transport mediated by interactions (cf. Fig. 5). One can argue that generally the fTWA should be more accurate in 2D than 1D because the system is closer to the mean-field regime. So, even for $\alpha = 1$, we anticipate that the fTWA gives reliable results.

The qualitative and quantitative differences between the dynamics in spin and charge sectors originates because the disorder potential in the Hamiltonian (5) directly couples only to charge degrees of freedom (see the discussion in Sec. III). In other words, there are perfect correlations between the disorder potential acting on both spin components manifested in the SU(2) symmetry of the model in the spin sector. However, by also adding disorder in the spin channel, e.g., by considering an independent disorder potential for "up" and "down" spins, the dynamics of local charges and spins become equivalent, as is demonstrated in Fig. 7 (for a 1D system, see Ref. [29]). For these simulations, we used the independent disorder potential of the form

$$\sum_{i\sigma} \Delta_i \hat{n}_{i\sigma} \to \sum_{i\sigma} \Delta_{i\sigma} \hat{n}_{i\sigma}, \tag{17}$$

where $\Delta_{i\uparrow}$ and $\Delta_{i\downarrow}$ are independently distributed. This potential obviously breaks the SU(2) spin symmetry. The data presented in Fig. 7 were generated using the same initial conditions as before, starting from either CDW or SDW stripe configurations and following the imbalance functions $\bar{z}_C(t)$ and $\bar{z}_S(t)$. Apart from small differences at short times, we see that the imbalance decay in both sectors is nearly identical, which is contrasted to the slower decay of the charge

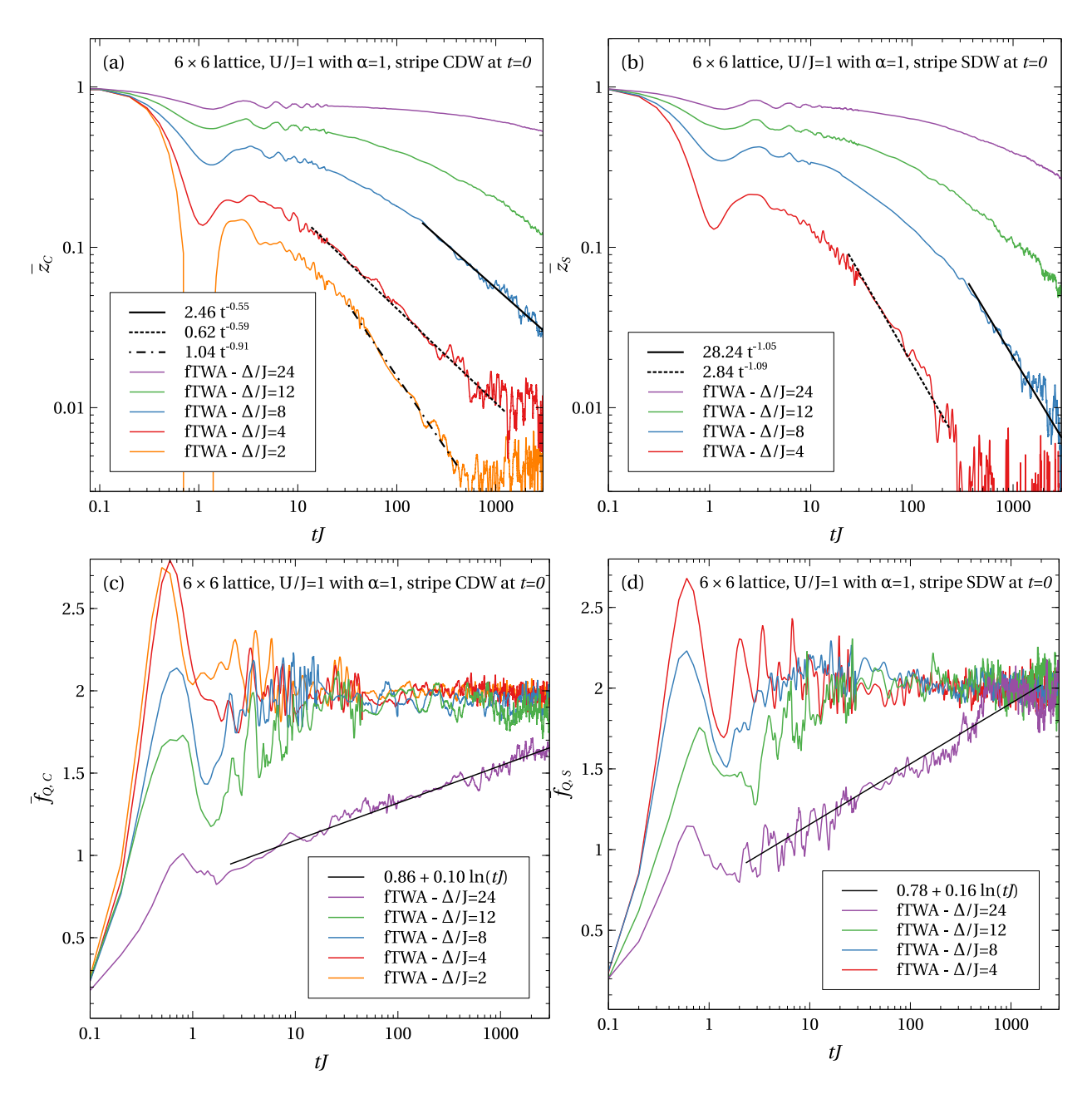


FIG. 5. Time dependence of (a),(b) the disorder-averaged charge $\bar{z}_C(t)$ and spin $\bar{z}_S(t)$ imbalance and (c),(d) the corresponding QFI for a 6 × 6 square lattice with the same on-site disorder for both spin components. (a),(c) The dynamics starting from the striped CDW initial state; (b),(d) the dynamics starting from the striped SDW initial state. Different colors represent different disorder strengths: $\Delta/J = 2$, 4, 8, 12, 24 [(a),(b) from bottom to top; (c),(d) from top to bottom]. The straight black lines show (a),(b) the best algebraic and (c),(d) the logarithmic fits to the long-time behavior of the corresponding imbalances and the QFI, respectively, and serve as a guide to the eye. All of the shown results were averaged over at least 20 different disorder realizations. The remaining parameters of the Hamiltonian are U/J = 1, $\alpha = 1$.

imbalance in the SU(2) case discussed above and shown for completeness in the inset of Fig. 7. This observation confirms that the difference of the dynamics in the charge and spin sectors in the system with the spin-independent (correlated) disorder is not due to the difference in initial conditions, but rather due to different thermalization mechanisms. One can also notice that with the uncorrelated disorder, decay of the charge and the spin imbalances is still subdiffusive with the exponent somewhat larger than for charge decay in the SU(2) regime (cf. the fitting curves in Figs. 5 and 7 for $\Delta/J=8$).

Let us note that in all of the simulations shown in this section, we used noise filtering to suppress the sampling noise, which is rather significant at long times. This noise goes down with the number of realizations of the initial conditions, but the convergence of the results is rather slow. We checked that the filtering we use does not introduce any systematic error and that the filtered fTWA accurately describes all nonspurious short-time oscillations of the observables. The effect of filtering on the charge imbalance together with the analysis of the finite-size effects is shown in Appendix C.

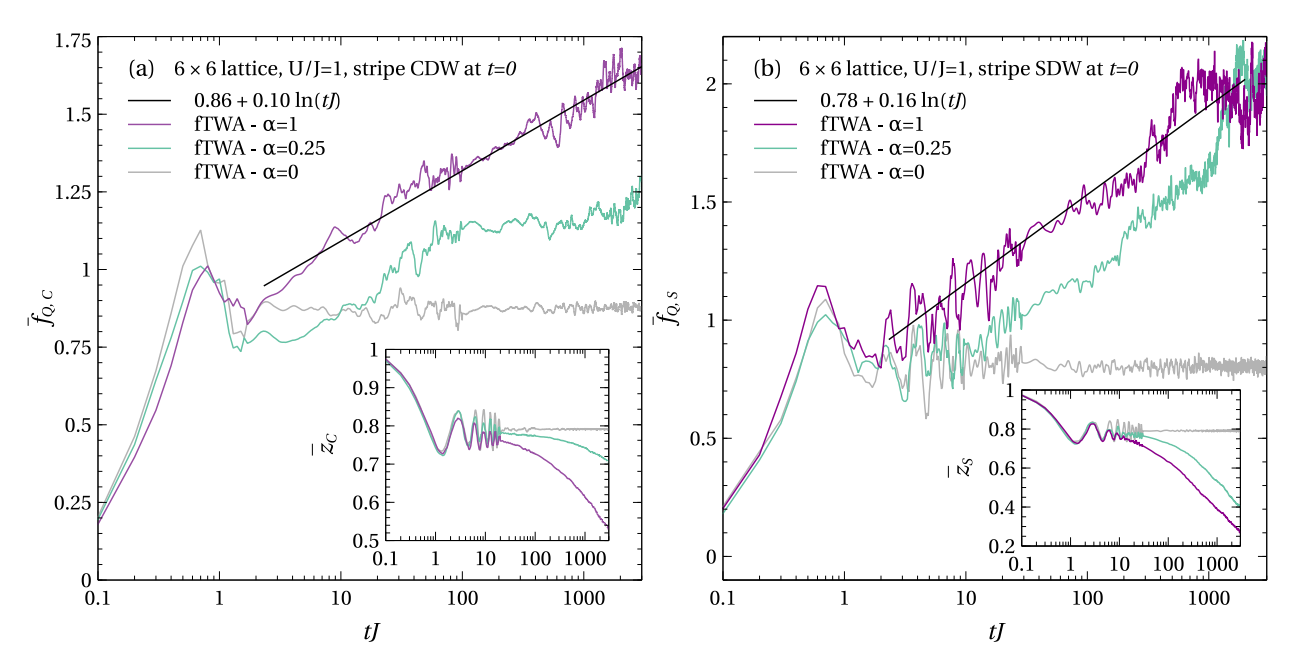


FIG. 6. Time dependence of the QFI density for a 6×6 lattice and the different values of $\alpha = 0, 0.25, 1$ (from bottom to top). The disorder and interaction strength are $\Delta/J = 24$, U/J = 1. The other parameters are the same as in Fig. 5. The systems are prepared in the striped (a) CDW and (b) SDW initial states. The black lines are the fits to the logarithmic time dependence. The insets show the time decay of the charge (spin) imbalance for $\alpha = 0, 0.25, 1$ (from top to bottom).

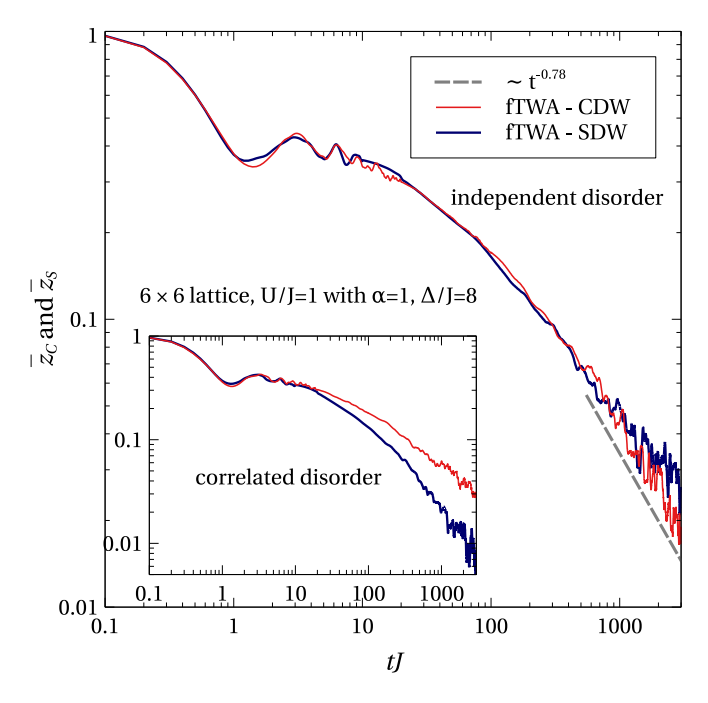
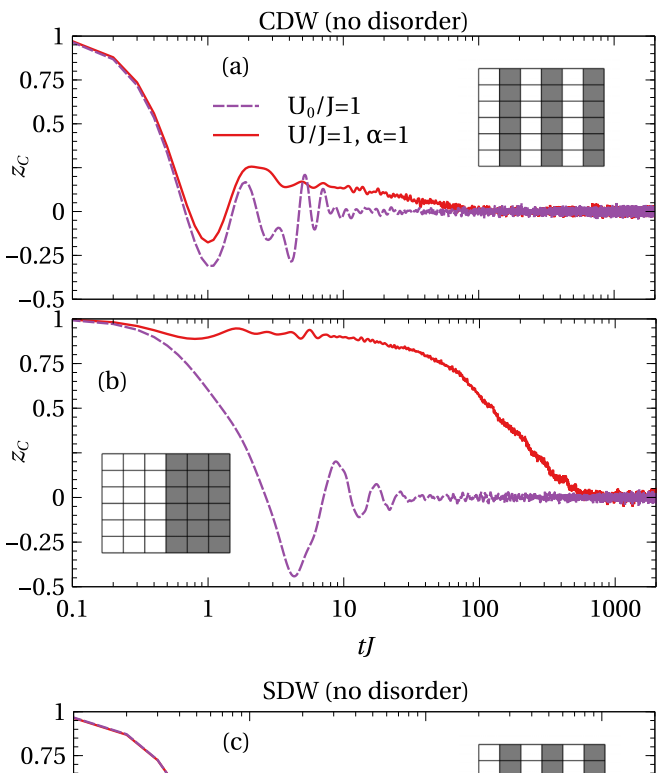


FIG. 7. Decay of charge and spin imbalance for the uncorrelated disorder potential for each spin component. The red (light gray) and blue (dark gray) lines represent the system initially prepared in the striped CDW and SDW state, respectively. The gray dashed line with algebraic time dependence is a guide for the eye for the best fit of the long-time imbalance to a power law. The disorder strength is $\Delta/J=8$ and the remaining parameters are the same as in Fig. 5. The inset shows the same results, but for a spin-independent disorder potential

V. MEMORY EFFECTS FOR DIFFERENT INITIAL STATES

Up to now, we analyzed a particular striped CDW or SDW initial state and saw how the presence of disorder slows down the dynamics in the system. In the absence of disorder, the system is expected to quickly thermalize, as illustrated in Figs. 8(a) and 8(c). Interestingly, in the long-range model, the thermalization time strongly depends on the initial state. This is easily seen by changing the initial CDW or SDW stripe width from the unit length to the half of the system size and by analyzing the corresponding imbalance functions, which are adjusted according to the width of the initial configuration. For clarity, we represent these initial states in the insets of Fig. 8, i.e., doubly occupied or empty (up or down) sites are depicted as a shadow or empty boxes for the CDW (SDW) initial states, respectively. As we can see, for newly introduced initial conditions [Figs. 8(b) and 8(d)], the thermalization time for charge degrees of freedom becomes significantly longer than for the striped initial configuration with the unit width [Figs. 8(a) and 8(c)]. In particular, we observe that for the single domain-wall initial state (i.e., for CDW or SDW stripe with the width of half of the system size), the timescale at which the charge imbalance $z_C(t)$ decays to zero is around $tJ \approx 700$ [Fig. 8(b)]. A qualitatively similar slowing down in a fermionic system with long-range hopping was numerically observed in Ref. [39]. We contrast the above results with those for the short-range interacting model with only on-site interactions between "up" and "down" species of strength U_0 (dashed purple lines), where the difference between the thermalization times for these two initial configurations is much less pronounced. Qualitatively, this long-memory effect can be explained by a high energy released by the particles traveling from the filled to the empty part of the system in the presence of long-range interactions. This energy has to be



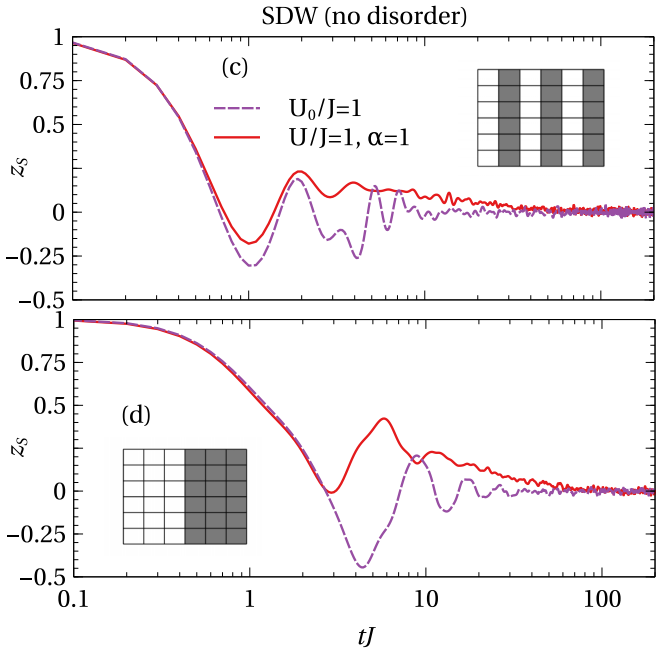


FIG. 8. Imbalance dynamics for short-range $(U_0/J=1)$ and long-range $(U/J=1, \alpha=1)$ interactions with different initial conditions. Stripes in the initial conditions are (a),(c) width 1 and (b),(d) width 3 (see insets). Simulations are performed for a nondisordered 6×6 lattice. Stripes contain doublons (spin-up) or empty (spin-down) sites when the system starts from the CDW (SDW) initial condition. Doublons or spin-up states in the initial conditions are denoted as shadow regions in the insets.

redistributed among the other degrees of freedom, resulting in a large kinematic barrier and hence in a smaller decay rate. As one can see from Figs. 8(c) and 8(d), the long-memory effect is absent, or at least is much weaker, for the SDW initial state.

To confirm the observed slowdown of thermalization of the charge sector in the long-range model, we perform the ED simulations in small systems and contrast them with the fTWA simulations. In Figs. 9(a) and 9(b), we analyze the charge imbalance decay for the domain-wall initial state for systems of sizes 8×1 and 4×2 , respectively. The initial state corresponds to the empty left half of the system and the fully occupied by doublons right half of the system. We see that long-range interactions lead to a slower thermalization rate of the charge imbalance compared to the short-range model, though the effect is not as strong as for larger system sizes analyzed in Fig. 8. At the same time, there is a little effect of the initial state on the decay of the SDW state [Fig. 9(c)], again in agreement with the earlier fTWA results for larger system sizes. From the comparison of the fTWA and the ED predictions in small systems, we see that the agreement is very good, especially for the long-range interactions and thus the fTWA simulations lead to reliable predictions. In Fig. 10, we analyze how the decay of the charge imbalance depends on the width of the system, which is gradually increased from $L_{\rm v}=1$ to $L_{\rm v}=4$. We see that there is a dramatic jump in the relaxation time as the width increases from 1 to 2, followed by its more gradual dependence if the width increases further. In the inset, we show that there is a very small effect of the width on the relaxation time for the short-range model.

Interestingly, in the presence of stronger disorder, slowing down of the thermalization by long-range interactions gets smaller and the equilibration timescales for the models with short-range and long-range interactions become comparable. This is illustrated in Fig. 11, where we compare imbalance decay for short- and long-range interactions (dashed and solid lines, respectively) for two different initial states (striped CDW [Fig. 11(a)] and domain wall [Fig. 11(b)]) and different disorder strengths. We see that only for a small disorder $\Delta/J = 2$, there is a very significant slowing down of the imbalance decay in the long-range model and for the domainwall initial state [two lowest lines in Fig. 11(b)]. Our findings suggest that extracting a potential many-body localization transition in the system with long-range interactions in a 2D lattice using the experimental protocol proposed in Ref. [2] requires extra care with choosing a proper initial state.

VI. SUMMARY

In this work, we developed an efficient semiclassical fTWA representation of dynamics in a Hubbard model with long-range interactions. The method is based on the proper phase-space representation of the Hubbard Hamiltonian. In particular, we resolved the ambiguity of finding the Weyl symbol of the Hamiltonian coming from the operator identity $\hat{n}_{\alpha}^2 = \hat{n}_{\alpha}$. We showed that this ambiguity can be eliminated by requiring that the fTWA becomes exact in the limit of the infinite-range interactions. We showed that using the corresponding Weyl symbol of the Hamiltonian in the presence of algebraically decaying interactions significantly improves the accuracy of the fTWA over a more naive choice of the Hamiltonian's phase-space representation.

Using the developed formalism, we applied the fTWA to study quench dynamics in the fermionic Hubbard model with long-range interactions in the presence of disorder. We first benchmarked the method against the ED results in small one-dimensional systems and then applied the

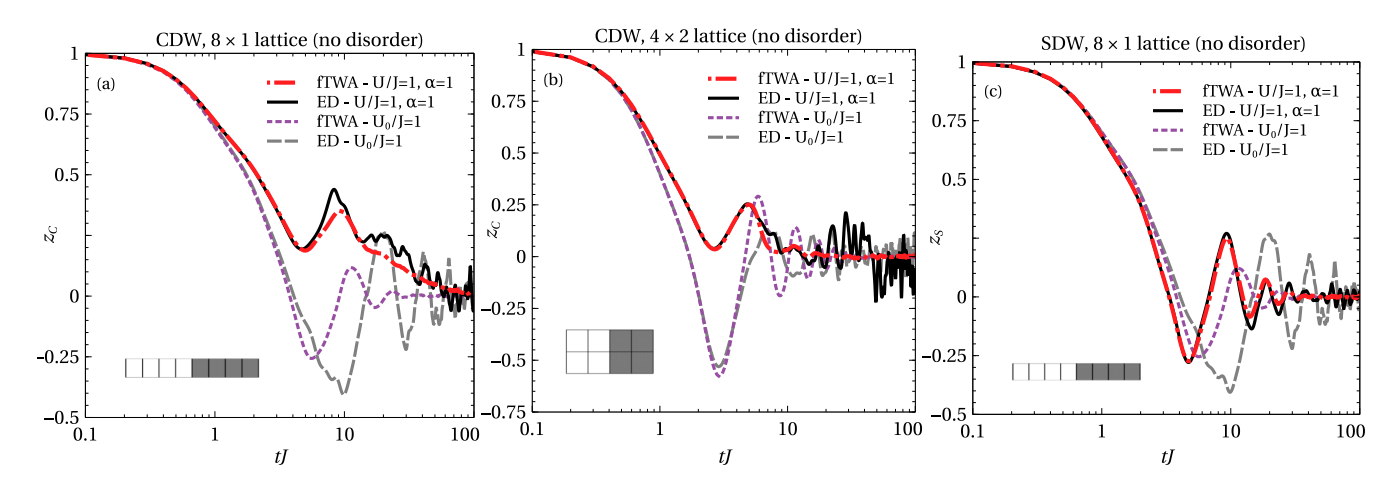


FIG. 9. Imbalance dynamics for small systems with short-range $(U_0/J=1)$ and long-range $(U/J=1, \alpha=1)$ interactions with domain-wall initial conditions (see text for details). The simulations are performed for nondisordered (a),(c) 8×1 and (b) 4×2 lattices. (a),(b) The initial CDW state; (c) the initial SDW state.

fTWA to a two-dimensional model, which is far beyond the reach of ED. In particular, motivated by recent experiments and theoretical works related to the Hubbard model [1,4,8,9,15,20,21,23,29,38], we analyzed the dynamics of charge and spin imbalance at half filling for different CDW-and SDW-type initial states and different disorder strengths. We showed that the fTWA can clearly distinguish different thermalization timescales of the charge and spin imbalance when the disorder potential is spin independent. In particular, even for the weak and moderate disorder potentials, we obtained subdiffusive charge transport characterized by

a power-law decay of the charge imbalance with a disorder-dependent exponent. At the same time, the spin transport under the same conditions remained diffusive. This anisotropy between charge and spin transport is consistent with earlier studies in one-dimensional systems [23,29–33,35–38]. We also showed that fTWA can accurately reproduce the QFI and found that it grows logarithmically in time at strong disorder. Moreover, we found that its growth rate is smaller for the QFI associated with the charge imbalance. This observation is consistent with slower charge transport and indicates that

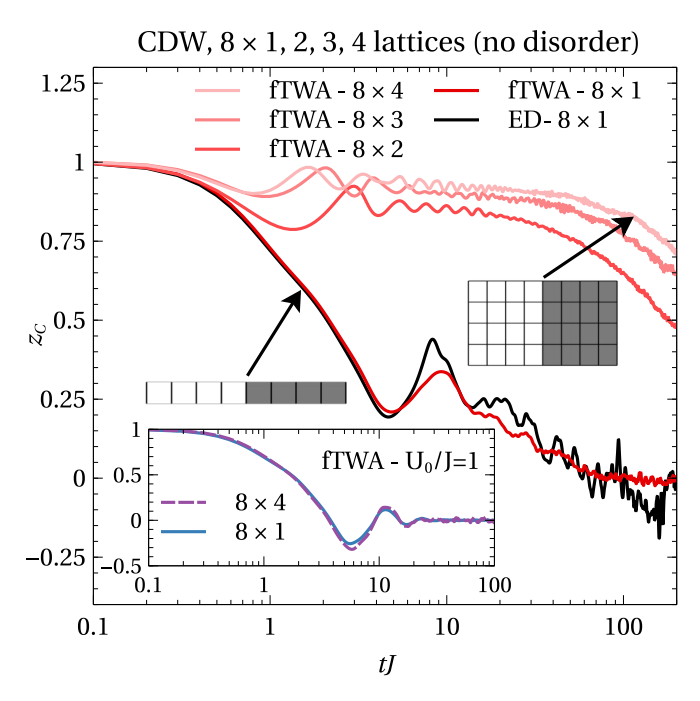


FIG. 10. The charge imbalance dynamics for nondisordered systems of a fixed length $L_x = 8$ and different width $L_y = 1, 2, 3, 4$ with long-range interactions $(U/J = 1, \alpha = 1)$ and the domain-wall CDW initial condition. The inset shows imbalance decay for 8×1 and 8×4 lattices with on-site interactions strength $U_0/J = 1$.

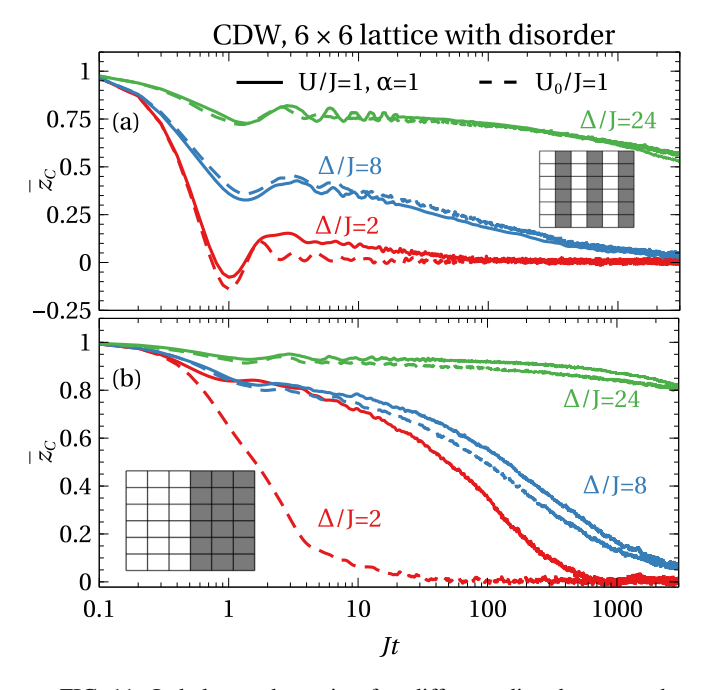


FIG. 11. Imbalance dynamics for different disorder strengths $(\Delta/J=2,~8,~24)$ and different interaction profiles: short-range interactions with $U_0/J=1$ (dashed lines) and long-range interactions with U/J=1 and $\alpha=1$ (solid lines). (a) The initial striped CDW state (width of stripe is 1); (b) the initial domain-wall state (width of CDW stripe is 3). The system size is 6×6 .

the information also spreads more slowly in the charge sector. We also investigated the role of different initial conditions and found that for long-range interactions, there is an additional and very strong mechanism, which suppresses thermalization of the initial domain-wall-type CDW state, i.e., the state where all doubly occupied sites are initially clustered together, even at weak disorder. This effect can be important for properly designing experimental protocols, which aim to detect potential localization transition in the systems with long-range interactions.

ACKNOWLEDGMENTS

We would like to thank Jonathan Wurtz and Markus Schmitt for valuable discussions. A.S.S. acknowledges funding from the Polish Ministry of Science and Higher Education through a "Mobilność Plus" Program No. 1651/MOB/V/2017/0. A.P. were supported by NSF Grant No. DMR-1813499 and AFOSR Grant No. FA9550-16-1-0334. We are also thankful for use of the facilities of the Boston University Shared Computing Cluster, over which we ran all the numerical simulations.

APPENDIX A: FERMIONIC TRUNCATED WIGNER APPROXIMATION (fTWA)

Here, we will summarize the main ideas of the fTWA formalism and its implementation. Additional details can be found in Refs. [39,40]. The fTWA formalism is a direct generalization of the standard TWA to fermionic systems, where $\rho_{\alpha\beta}=\rho_{\beta\alpha}^*$, $\tau_{\alpha\beta}^*$, $\tau_{\alpha\beta}^*$ play the role of the complex phase-space variables (for their definition, see Sec. II). All observables including the Hamiltonian and the initial density matrix are represented by these phase-space variables. However, as mentioned in Sec. II, one can consider Hamiltonian dynamics within ρ representation which restrict phase-space parametrization to $\rho_{\alpha\beta}$ variables only. Then, the expectation value of some time-dependent observable in the Heisenberg representation $\hat{\mathcal{O}}(t)$ within the fTWA is evaluated in the following way:

$$\langle \hat{\mathcal{O}}(t) \rangle = \int d\boldsymbol{\rho}_0 W(\boldsymbol{\rho}_0) \mathcal{O}_W(\boldsymbol{\rho}(t)),$$
 (A1)

where W is the Wigner function, \mathcal{O}_W is the Weyl symbol of the operator $\hat{\mathcal{O}}$, and $\rho = \{\rho_{\alpha\beta} : \alpha, \beta \in \{1, ..., N\}\}$. Here the integration is performed over the initial conditions, with the Wigner function $W(\rho_0)$ playing the role of their probability distribution. Following Refs. [39,40], we approximate the Wigner function with a positive Gaussian distribution, which correctly reproduces both the expectation values of the phase-space variables and their fluctuations in the initial state. Such positive representation is always possible for any Slater-determinant-type initial state and is likely possible for other states. In particular, the CDW and SDW initial states that are analyzed in this work, and which are straightforward to realize in cold atoms [1,2,4,8,9], belong to this category. We note that it is the presence of fluctuations encoded in the Wigner function that makes the fTWA fundamentally different from mean field and allows one to extract such purely quantum observables as the QFI. In order to find $\rho(t)$ entering Eq. (A1), one has to solve the deterministic classical and generally nonlinear equations of motion,

$$\frac{\partial \rho_{\alpha\beta}}{\partial t} = \{\rho_{\alpha\beta}, H_W\} \equiv \sum_{\mu\nu\gamma\delta} f(\alpha, \beta, \mu, \nu, \gamma, \delta) \frac{\partial H_W}{\partial \rho_{\mu\nu}} \rho_{\gamma,\delta}, \quad (A2)$$

satisfying the randomly sampled initial conditions: $\rho(t=0) = \rho_0$. The evolution is governed by H_W , which plays the role of the classical Hamiltonian. We discuss the two possible choices for H_W corresponding to the Hamiltonians \hat{H}_I [Eq. (4)] and \hat{H}_{II} [Eq. (5)] in Appendix B [cf. Eqs. (B1) and (B2)]. Finally, f in the equation of motion define the structure constants, which in turn define the Poisson brackets of the classical Hamiltonian evolution. These structure constants are found from the commutation relations,

$$\left[\hat{E}^{\alpha}_{\beta}, \, \hat{E}^{\mu}_{\nu}\right] = i \sum_{\nu \delta} f(\alpha, \beta, \mu, \nu, \gamma, \delta) \hat{E}^{\gamma}_{\delta}, \tag{A3}$$

and are easy to compute [39]. Instead of listing them here in Appendix B, we show the explicit form of Eq. (A2) for the two choices of the Hamiltonian, \hat{H}_I and \hat{H}_{II} .

APPENDIX B: SEMICLASSICAL EQUATIONS OF MOTION FOR \hat{H}_I AND \hat{H}_{II}

The Weyl symbols of the Hamiltonians \hat{H}_I and \hat{H}_{II} can be found by standard means using the Bopp representation of the operators $\hat{\rho}_{\alpha\beta}$ [39],

$$H_{I,W} = -J \sum_{\langle ij \rangle} \rho_{i\sigma j\sigma} + \sum_{i\sigma} \Delta_i \rho_{i\sigma i\sigma} + \sum_{ij} U_{ij} \left(\rho_{i\uparrow i\uparrow} + \frac{1}{2} \right) \left(\rho_{j\downarrow j\downarrow} + \frac{1}{2} \right) + \sum_{i < j,\sigma} V_{ij\sigma} \left(\rho_{i\sigma i\sigma} + \frac{1}{2} \right) \left(\rho_{j\sigma j\sigma} + \frac{1}{2} \right), \quad (B1)$$

$$H_{II,W} = -J \sum_{\langle ij \rangle} \rho_{i\sigma j\sigma} + \sum_{i\sigma} \Delta_i \rho_{i\sigma i\sigma} + \sum_{ij} U_{ij} \left(\rho_{i\uparrow i\uparrow} + \frac{1}{2} \right) \left(\rho_{j\downarrow j\downarrow} + \frac{1}{2} \right) + \frac{1}{2} \sum_{i,j,\sigma} V_{ij\sigma} \left(\rho_{i\sigma i\sigma} + \frac{1}{2} \right) \left(\rho_{j\sigma j\sigma} + \frac{1}{2} \right). \tag{B2}$$

Then the corresponding equations of motion for the $\rho_{\alpha\beta}$ variables [see Eq. (A2)] read

$$i\frac{\partial \rho_{m\sigma n\sigma}}{\partial t} = -J \sum_{\delta} (\rho_{m\sigma,n+\delta \sigma} - \rho_{m+\delta \sigma,n\sigma}) + \rho_{m\sigma n\sigma} \left[(\Delta_n - \Delta_m) + \sum_r (U_{nr} - U_{mr}) \left(\rho_{r-\sigma r-\sigma} + \frac{1}{2} \right) \right]$$
$$+ \rho_{m\sigma n\sigma} \sum_r \left[(1 - \delta_{nr}) V_{nr\sigma} - (1 - \delta_{mr}) V_{mr\sigma} \right] \left(\rho_{r\sigma r\sigma} + \frac{1}{2} \right), \quad H = H_{I,W},$$
(B3)

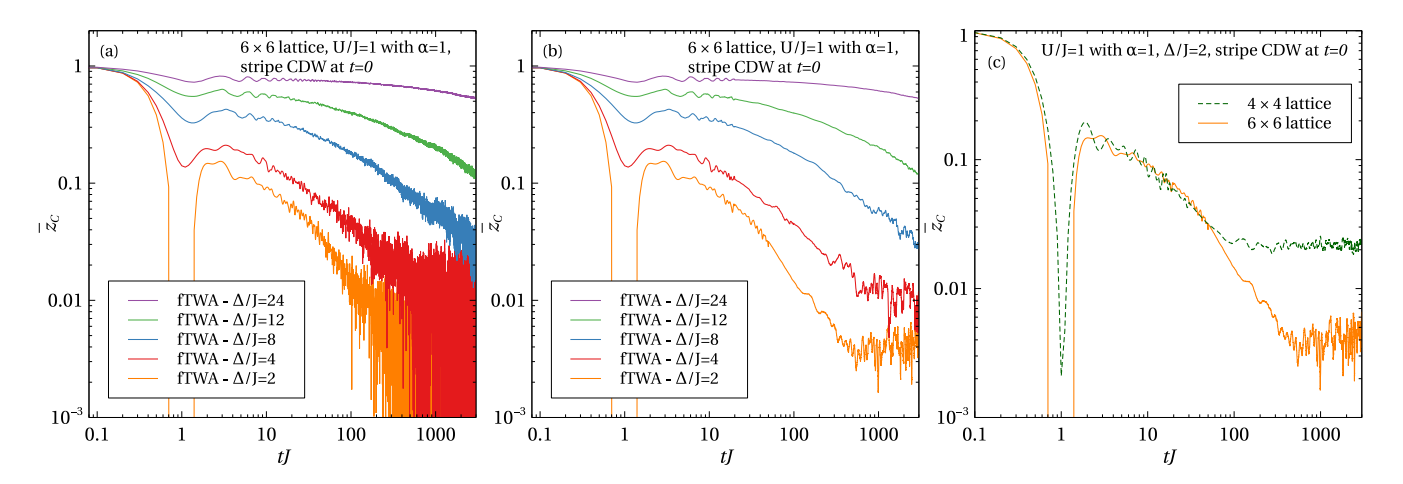


FIG. 12. Long-time dynamics of the charge imbalance $\bar{z}_C(t)$. (a) Unfiltered data; (b) the same data after filtering. The parameters used for the simulations are U/J=1, $\alpha=1$, and the lattice size is 6×6 . The results are averaged over at least 20 different disorder realizations. (a),(b) Different colors represent different disorder strengths: $\Delta/J=2$, 4, 8, 12, 24 (from bottom to top). (c) The dynamics of the charge imbalance for two different system sizes 4×4 and 6×6 , suggesting that the long-time saturation of the imbalance at a small but nonzero value is a finite-size effect.

and

$$i\frac{\partial \rho_{m\sigma n\sigma}}{\partial t} = -J \sum_{\delta} (\rho_{m\sigma,n+\delta \sigma} - \rho_{m+\delta \sigma,n\sigma}) + \rho_{m\sigma n\sigma} \left[(\Delta_n - \Delta_m) + \sum_r (U_{nr} - U_{mr}) \left(\rho_{r-\sigma r-\sigma} + \frac{1}{2} \right) \right]$$

$$+ \rho_{m\sigma n\sigma} \sum_{\delta} (V_{nr\sigma} - V_{mr\sigma}) \left(\rho_{r\sigma r\sigma} + \frac{1}{2} \right), \quad H = H_{II,W}.$$
(B4)

These equations are similar but not equivalent. In the limit of the infinite-range interactions, where $U_{ij} = U$ and $V_{ij\sigma} = V$, Eqs. (B3) and (B4) simplify to

$$i\frac{\partial \rho_{m\sigma n\sigma}}{\partial t} = -J\sum_{\delta} \left(\rho_{m\sigma,n+\delta \sigma} - \rho_{m+\delta \sigma,n\sigma}\right) + (\Delta_n - \Delta_m)\rho_{m\sigma n\sigma} + V\rho_{m\sigma n\sigma}\sum_{r} \left(\delta_{mr} - \delta_{nr}\right) \left(\rho_{r\sigma r\sigma} + \frac{1}{2}\right)$$
(B5)

and

$$i\frac{\partial \rho_{m\sigma n\sigma}}{\partial t} = -J \sum_{\delta} \left(\rho_{m\sigma, n+\delta \sigma} - \rho_{m+\delta \sigma, n\sigma} \right) + (\Delta_n - \Delta_m) \rho_{m\sigma n\sigma}.$$
 (B6)

We see that the first system of equations, which was obtained using $H_{I,W}$, still contains nonlinear terms, while the second system of equations based on the $H_{II,W}$ representation of the Hamiltonian is linear, which has to be the case because the full quantum evolution is linear. Mathematically, the origin of ambiguity comes from the fact that the operator identity for fermions $\hat{n}_{\alpha}^2 = \hat{n}_{\alpha}$, which does not follow from the properties of the U(N) algebra used to define the Poisson brackets, but rather from the fact that the operators \hat{E}^{α}_{β} form a particular fundamental representation of this algebra. At the same time, the Weyl phase-space mapping of the operators is independent of the particular representation.

APPENDIX C: NOISE AND FINITE-SIZE EFFECTS IN FTWA SIMULATIONS

In Figs. 12(a) and 12(b), we show the charge imbalance before and after removing substantial sampling noise from the fTWA simulations. For each disorder realization of fTWA simulations on a 6×6 lattice, we use at least 20 different trajectories corresponding to different random initial conditions. This number is to be contrasted with averaging over 400 realization in Sec. III, where we benchmarked the fTWA against the exact results in small systems. While averaging over 20 different initial conditions is sufficient to obtain a smooth short-time behavior of the imbalance, more

averaging is needed to eliminate the sampling noise at long times. Because even classical simulations in large systems are computationally costly, we found that it is more efficient to apply filtering to the imbalance data to suppress this long-time spurious noise. As is evident from comparing the curves shown in Figs. 12(a) and 12(b), the filtering does not introduce any systematic error.

In Fig. 12(c), we analyze finite-size effects on the imbalance dynamics by comparing the fTWA simulations for two different system sizes 4×4 and 6×6 . We see that apart from a small difference in the first oscillation (enhanced in the plot because of using the logarithmic scale), the results for the two

system sizes are very similar until the imbalance saturates at long times at a small positive value, which rapidly goes to zero with the system size. From this comparison, we can conclude that the 6×6 system size is sufficient to capture some key features of the imbalance dynamics in the thermodynamic limit

- [1] M. Schreiber, S. S. Hodgman, P. Bordia, H. P. Lüschen, M. H. Fischer, R. Vosk, E. Altman, U. Schneider, and I. Bloch, Science 349, 842 (2015).
- [2] J. y. Choi, S. Hild, J. Zeiher, P. Schauss, A. Rubio-Abadal, T. Yefsah, V. Khemani, D. A. Huse, I. Bloch, and C. Gross, Science 352, 1547 (2016).
- [3] J. Smith, A. Lee, P. Richerme, B. Neyenhuis, P. W. Hess, P. Hauke, M. Heyl, D. A. Huse, and C. Monroe, Nat. Phys. 12, 907 (2016).
- [4] P. Bordia, H. P. Lüschen, S. S. Hodgman, M. Schreiber, I. Bloch, and U. Schneider, Phys. Rev. Lett. 116, 140401 (2016)
- [5] J. Zhang, P. W. Hess, A. Kyprianidis, P. Becker, A. Lee, J. Smith, G. Pagano, I.-D. Potirniche, A. C. Potter, A. Vishwanath, N. Y. Yao, and C. Monroe, Nature (London) 543, 217 (2017).
- [6] S. Choi, J. Choi, R. Landig, G. Kucsko, H. Zhou, J. Isoya, F. Jelezko, S. Onoda, H. Sumiya, V. Khemani, C. von Keyserlingk, N. Y. Yao, E. Demler, and M. D. Lukin, Nature (London) 543, 221 (2017).
- [7] H. P. Lüschen, P. Bordia, S. S. Hodgman, M. Schreiber, S. Sarkar, A. J. Daley, M. H. Fischer, E. Altman, I. Bloch, and U. Schneider, Phys. Rev. X 7, 011034 (2017).
- [8] H. P. Lüschen, P. Bordia, S. Scherg, F. Alet, E. Altman, U. Schneider, and I. Bloch, Phys. Rev. Lett. 119, 260401 (2017).
- [9] P. Bordia, H. Lüschen, S. Scherg, S. Gopalakrishnan, M. Knap, U. Schneider, and I. Bloch, Phys. Rev. X 7, 041047 (2017).
- [10] G. Kucsko, S. Choi, J. Choi, P. C. Maurer, H. Zhou, R. Landig, H. Sumiya, S. Onoda, J. Isoya, F. Jelezko, E. Demler, N. Y. Yao, and M. D. Lukin, Phys. Rev. Lett. 121, 023601 (2018).
- [11] A. Lukin, M. Rispoli, R. Schittko, M. E. Tai, A. M. Kaufman, S. Choi, V. Khemani, J. Léonard, and M. Greiner, Science 364, 256 (2019).
- [12] B. Chiaro, C. Neill, A. Bohrdt, M. Filippone, F. Arute, K. Arya, R. Babbush, D. Bacon, J. Bardin, R. Barends *et al.*, arXiv:1910.06024.
- [13] R. Nandkishore and D. A. Huse, Annu. Rev. Condens. Matter Phys. 6, 15 (2015).
- [14] D. A. Abanin, E. Altman, I. Bloch, and M. Serbyn, Rev. Mod. Phys. 91, 021001 (2019).
- [15] T. Kohlert, S. Scherg, X. Li, H. P. Lüschen, S. Das Sarma, I. Bloch, and M. Aidelsburger, Phys. Rev. Lett. 122, 170403 (2019).
- [16] D. J. Luitz and Y. B. Lev, Ann. Phys. **529**, 1600350 (2017).
- [17] M. Žnidarič, T. Prosen, and P. Prelovšek, Phys. Rev. B 77, 064426 (2008).
- [18] J. H. Bardarson, F. Pollmann, and J. E. Moore, Phys. Rev. Lett. 109, 017202 (2012).
- [19] M. Serbyn, Z. Papić, and D. A. Abanin, Phys. Rev. Lett. 110, 260601 (2013).

- [20] G. De Tomasi, F. Pollmann, and M. Heyl, Phys. Rev. B 99, 241114(R) (2019).
- [21] M. Pino, Phys. Rev. B 90, 174204 (2014).
- [22] R. Singh, R. Moessner, and D. Roy, Phys. Rev. B 95, 094205 (2017).
- [23] B. Pandey and S. K. Pati, arXiv:1905.06677.
- [24] G. De Tomasi, Phys. Rev. B 99, 054204 (2019).
- [25] A. Safavi-Naini, M. L. Wall, O. L. Acevedo, A. M. Rey, and R. M. Nandkishore, Phys. Rev. A 99, 033610 (2019).
- [26] M. Pollak, *The Electron Glass* (Cambridge University Press, Cambridge, 2013).
- [27] V. N. Kotov, B. Uchoa, V. M. Pereira, F. Guinea, and A. H. Castro Neto, Rev. Mod. Phys. 84, 1067 (2012).
- [28] A. Altland and B. D. Simons, *Condensed Matter Field Theory* (Cambridge University Press, Cambridge, 2010).
- [29] P. Prelovšek, O. S. Barišić, and M. Žnidarič, Phys. Rev. B 94, 241104(R) (2016).
- [30] M. Mierzejewski, M. Kozarzewski, and P. Prelovšek, Phys. Rev. B 97, 064204 (2018).
- [31] M. Kozarzewski, P. Prelovšek, and M. Mierzejewski, Phys. Rev. Lett. 120, 246602 (2018).
- [32] X. Yu, D. Luo, and B. K. Clark, Phys. Rev. B 98, 115106 (2018).
- [33] J. Wurtz, P. W. Claeys, and A. Polkovnikov, Phys. Rev. B 101, 014302 (2020).
- [34] U. Krause, T. Pellegrin, P. W. Brouwer, D. A. Abanin, and M. Filippone, arXiv:1911.11711.
- [35] B. Leipner-Johns and R. Wortis, Phys. Rev. B 100, 125132 (2019).
- [36] M. Środa, P. Prelovšek, and M. Mierzejewski, Phys. Rev. B 99, 121110(R) (2019).
- [37] J. Zakrzewski and D. Delande, Phys. Rev. B 98, 014203 (2018).
- [38] I. V. Protopopov and D. A. Abanin, Phys. Rev. B **99**, 115111 (2019).
- [39] S. M. Davidson, D. Sels, and A. Polkovnikov, Ann. Phys. 384, 128 (2017).
- [40] M. Schmitt, D. Sels, S. Kehrein, and A. Polkovnikov, Phys. Rev. B 99, 134301 (2019).
- [41] G. I. Japaridze and A. P. Kampf, Phys. Rev. B 59, 12822 (1999).
- [42] J. R. Garrison, R. V. Mishmash, and M. P. A. Fisher, Phys. Rev. B 95, 054204 (2017).
- [43] P. W. Anderson, Phys. Rev. 109, 1492 (1958).
- [44] D. Basko, I. Aleiner, and B. Altshuler, Ann. Phys. 321, 1126 (2006).
- [45] A. Pal and D. A. Huse, Phys. Rev. B 82, 174411 (2010).
- [46] S. L. Braunstein and C. M. Caves, Phys. Rev. Lett. 72, 3439 (1994).
- [47] P. Hyllus, W. Laskowski, R. Krischek, C. Schwemmer, W. Wieczorek, H. Weinfurter, L. Pezzé, and A. Smerzi, Phys. Rev. A 85, 022321 (2012).
- [48] G. Tóth, Phys. Rev. A 85, 022322 (2012).

- [49] P. Hauke, M. Heyl, L. Tagliacozzo, and P. Zoller, Nat. Phys. 12, 778 (2016).
- [50] O. L. Acevedo, A. Safavi-Naini, J. Schachenmayer, M. L. Wall, R. Nandkishore, and A. M. Rey, Phys. Rev. A 96, 033604 (2017).
- [51] J. Wurtz, A. Polkovnikov, and D. Sels, Ann. Phys. 395, 341 (2018).
- [52] V. Oganesyan, A. Pal, and D. A. Huse, Phys. Rev. B 80, 115104 (2009).
- [53] A. K. Kulshreshtha, A. Pal, T. B. Wahl, and S. H. Simon, Phys. Rev. B 98, 184201 (2018).
- [54] Y. B. Lev and D. R. Reichman, Europhys. Lett. **113**, 46001 (2016).